Eur. Phys. J. B **4**, 279–284 (1998)

THE EUROPEAN PHYSICAL JOURNAL B

Simulated mesoscopic structures of a domain wall in a ferroelastic lattice

J. Novak[a] and E.K.H. Salje

Department of Earth Sciences, University of Cambridge, Downing Street, Cambridge, CB2 3EQ, UK

Received: 20 March 1998 / Received in final form and Accepted: 7 May 1998

Abstract. A precise description of the twin domain wall in a ferroelastic lattice is presented. The bulk structure of the wall is described by the Landau-Ginzburg model, with and without the fourth order spatial derivative of the order parameter. The domain wall at the surface is seen as a rounded ridge, with the characteristic thickness of the ridge being the same as the thickness of the wall in the bulk. The elastic response of the surface close to the wall is rather exotic. We predict that the AFMTM images should show a narrow groove in the middle of the ridge with two hill-like features on either side of the groove. Consequences for the chemical activity of the surface for the sites close to the wall are discussed.

PACS. 62.90.+k Other topics in mechanical and acoustical properties of condensed matter – 62.20.-x Mechanical properties of solids – 77.80.Dj Domain structure; hysteresis

1 Introduction

Ferroelastic domains are both desirable and common features occurring in materials and minerals. Almost all ferroelastic or co-elastic materials exhibit domain patterns when they go through a structural phase transition, and these domain patterns influence their physical properties [1]. During the phase transition which is nearly continuous, characteristic twinning and/or tweeding processes occur. While single-domain samples are possible to produce under special conditions, it is difficult to exclude domain walls through available techniques such the application of as uniaxial stress [2–4]. The formation of microstructure is usually spontaneous, but domains can also originate from some external field exerted on the sample. The thermodynamic description of these processes is well-understood [5–9]. This description, though, does not provide a precise determination of the structure on a mesoscopic scale.

Such microstructure is rich in mesoscopic structures which are difficult to investigate experimentally. Although the twin domain walls, which are the building blocks of the mesoscopic structures, appear as distinct features in images obtained with transition electron microscopy (TEM) techniques [10], the preparation of the samples as thin slabs or wedges for use with TEM significantly alters any fine structure present. Recently, microstructure has been studied by a more subtle mode of investigation, the high-resolution X-ray diffraction which directly observes the diffuse scattering around Bragg reflections [11]. The diffuse diffraction profiles can in most cases be correlated to some mesoscopic structure characteristics, *e.g.* the width of domain walls. Although the sensitivity of this technique is relatively good (identification of wall patterns with one wall in 10 000 Å), it does not provide us with much more [12,13]. The more complex details of the mesoscopic structures, such as the surface structures and needle tips are still not accessible, mainly due to the fact that the X-ray diffraction studies give bulk properties, and we are interested in the description of mesoscopic structures, which are of local nature. Another possible mode of experimental investigation is by atomic force microscopy (AFM) or related techniques which are sensitive to the spatial variation of the surface topography or physical properties of material [14–17]. Besides the fact that these techniques can concentrate on the surface properties exclusively, thus excluding the determination of sub-surface or even bulk properties, they have not been successful in determining even that in sufficient detail.

The lack of reports on the details of the mesoscopic structures is in contrast with the importance they play in materials of interest. There are many examples of materials where the microstructure determines their physical properties, *e.g.* the current characteristics of the high-temperature superconductors are related to their mesoscopic structure. The surface reactivity of materials is found to be closely related to the surface microstructure and that relation has proved not to be straightforward. On another front, the analysis of mesoscopic structures of minerals has been used to determine the past geological events [18].

In this paper we present a precise description of the mesoscopic features around a twin domain wall, throughout the lattice.

[a] e-mail: jnovak@esc.cam.ac.uk

2 Simulation method

The model we use to simulate twin domains and mesoscopic structures of interest is a simple two-dimensional lattice that represents a hypothetical plane perpendicular to the twin walls that form the mesoscopic structures in the ferroelastic phase. The twin domains are generated by the elastic shear deformation of the square unit cells. Such deformation (*i.e.* spontaneous strain in a ferroelastic material) is rather common as previously noted, and provides a source for the formation of microstructure, in the case of our interest, ferroelastic twinning [1]. In our generic model [5,8] the lattice points interact with each other *via* elastic potentials.

Each point at the site (i, j) has two degrees of freedom, the two coordinates $X_{i,j}$ and $Y_{i,j}$. In order to generate surface relaxations, which were necessary to describe the surface behavior of mesoscopic structures, it is essential that interatomic interactions extend to, at least, two interatomic layers perpendicular to the surface [19]. Therefore, each lattice point (i, j) interacts explicitly with the points populating its third and lower coordination shells, and interactions for further neighbors are ignored. To successfully describe mesoscopic structures and their surface features, we needed to simulate only two free surfaces, those perpendicular to both the lattice plane simulated and to the non-deformed domain walls creating the mesoscopic structures. This approach yields three distinctive classes of points in the model, those in the bulk, interacting with twelve neighbors, then those in the layer next to the surface, interacting with eleven neighbors, and finally, the points in the surface layer having only eight neighbors to interact with. Lennard-Jones potentials are used for second and third nearest neighbor interactions, and harmonic potentials are used for nearest neighbor interactions. We used a harmonic potential in order to preserve the lattice configuration, effectively keeping the lattice parameter at a constant value throughout the simulation. The potential energy of a point (i, j) can be written as:

$$\mathcal{U}_p(i,j) = \sum_{n=1}^{p} \mathcal{U}_n(|\mathbf{r}|), \tag{1}$$

where the subscript p denotes the position of the point and the number of neighbors it interacts with:

$$p = \begin{cases} 12\text{: bulk} \\ 11\text{: next to surface} \\ 8\text{: surface,} \end{cases}$$

and $\mathcal{U}_n(|\mathbf{r}|)$ is:

$$\mathcal{U}_n(|\mathbf{r}|) = \begin{cases} \dfrac{1}{2}\,\kappa\,(|\mathbf{r}| - a)^2\text{:} & \text{nearest neighbors} \\ \varepsilon^* \left[\dfrac{r^{*12}}{|\mathbf{r}|^{12}} - 2\dfrac{r^{*6}}{|\mathbf{r}|^{6}} \right]\text{:} & \text{2nd nearest} \\ \varepsilon^* \left[\dfrac{s^{*12}}{|\mathbf{r}|^{12}} - 2\dfrac{s^{*6}}{|\mathbf{r}|^{6}} \right]\text{:} & \text{3rd nearest,} \end{cases}$$

where $\mathbf{r}$ is the distance vector, r^* and s^* are the positions of the Lennard-Jones potential minima, and κ and ε^* are the energy parameters, set to $\kappa = 2700$, $\varepsilon^* = 1$.

The ground state of the lattice is characterized by the shear angle, a function of r^*/a, and the lattice parameter, a function of ε^*/κ. If $r^* \geq a$, the shear angle is non zero. In that case, the second neighbors lie in the region where the second derivative of the Lennard-Jones potential is negative, and the energy of a sheared square is lower than that of an unsheared one. We chose the shear angle to be 3° ($r^* = 1.2864483$, $a = 1$), in agreement with some representative real materials [20]. The energy parameters were adjusted accordingly.

The choice of s^* influences the elastic anisotropy energy, which in turn is important in determination of the shapes of mesoscopic structures. The elastic anisotropy energy describes the excess energy of a straight part of a domain wall for orientations which are not along directions that are elastically soft.

Domain structures and surface relaxation were then calculated by numerical minimization of the total energy functional:

$$\delta \int dr^3 \left\{ \sum_{i,j} \mathcal{U}_p(i,j) \right\} = 0, \tag{2}$$

where $\mathcal{U}_p(i, j)$ is as defined in (1) and the sum extends over all lattice points.

A combination of two different boundary conditions was used in the simulation with free surface boundary conditions at the [01] and $[0\overline{1}]$ surfaces. The [10] and $[\overline{1}0]$ edges of the simulated lattice were treated with derivative boundary conditions. This can easily be extended to all three dimensions, if the complete lattice is assumed to be constructed of an infinite number of layers simulated here, extending in the [001] and $[00\overline{1}]$ directions. The indexing of the edges of the simulated lattice is then achieved by adding a third index $l = 0$ to the above expressions.

For elastic properties, the free surface boundary conditions might not seem appropriate, especially for nonlarge sizes of the simulated lattice, due to the long-range character of elastic forces. Since we were interested in surface properties of some mesoscopic structures in particular, we were forced to use the free surface boundary conditions, and avoid problems by choosing a lattice large enough to avoid the surface-surface interaction, but within the scope of the available hardware on which the simulation has been run.

The derivative boundary conditions were the simplest to mimic the infinite extension of the simulated lattice in the given direction. The particles at the edge of the lattice were displaced by the same amount from their nearest neighbors, as those were from their respective nearest neighbors in the lattice. By doing this, the derivative of the displacement with respect to the $\hat{x}$ spatial coordinate was kept constant. This was crucial to allow the lattice with its free surfaces to relax freely, uninfluenced by any anomalies, with the exception of the domain wall simulated.

The present model has been studied by the molecular dynamics technique. We have not included any thermodynamic fluctuations, and have effectively simulated a system far away from the ferroelastic-paraelastic transition temperature T_c. In order to study sets of twin walls creating the mesoscopic structures, without the influence of boundaries parallel to the walls and surface relaxation extending to $\sim 10\%$ of the sample, a minimum of 80 000 points were considered for a two-dimensional layer perpendicular to the surface and the twin walls.

Since the simulation is only dealing with real space positions $X_{i,j}$ and $Y_{i,j}$ of each point (i,j) in the lattice, the output is a set of coordinates. This data was then manipulated to yield the $(xx-yy)$ component of the strain field throughout the simulated relaxed lattice.

The production runs of the simulation were carried out on the Hitachi S-3600/180 vector supercomputer, a part of the Cambridge High Performance Computing Facility.

3 Twin domain wall in the bulk

Analytically, the ferroelastic materials have been well-described using Landau-Ginzburg phenomenological model, which expresses the Gibbs free energy as a polynomial in the order parameter and its spatial derivative [1]:

$$\begin{aligned} G = G_0 &+ \frac{1}{2}A\theta_s\left(\coth\frac{\theta_s}{T} - \coth\frac{\theta_s}{T_c}\right)\mathcal{Q}^2 + \frac{1}{4}B\mathcal{Q}^4 \\ &+ \frac{1}{6}C\mathcal{Q}^6 + \frac{1}{2}\Big[g(\nabla\mathcal{Q})^2 + g'(\nabla^2\mathcal{Q})^2\Big] + \lambda_i\mathcal{Q}e_i \\ &+ \frac{1}{2}\sum C_{ik}e_ie_k, \end{aligned} \tag{3}$$

where $\mathcal{Q}$ is the order parameter, θ_s is the saturation temperature of the order parameter, T_c is the critical temperature and e_i is the i-th component of the strain in Voigt notation. The strain component which is the order parameter in the ferroelastic phase transition is then treated as $\mathcal{Q}$. A domain wall is a low energy excitation of the system, and the total energy of the domain wall is minimized, with the conditions that, in general, no secondary strain fields are excited, and that no lattice imperfections occur. In our model, neither of these can happen, so the minimization takes the following form:

$$\delta\int dr\, G(r) = 0, \tag{4}$$

where $G(r)$ is the energy functional from equation (3), and r is the coordinate perpendicular to the wall. The boundary condition for minimization is the relation of the order parameters in the adjacent parts of the lattice, *i.e.* equal magnitude, opposite sign. The two adjacent domains are twin related, in our model, and in the most ferroelastics. The energy minimum can be obtained by solving equation (4) numerically, which we did in our simulation, or, analytically by solving the corresponding Euler-Lagrange differential equation. If we assume that $e\left(\mathcal{Q}(r)\right)$ is always fully relaxed, the functional $G\left(\mathcal{Q}, e_i, T\right)$ is reduced to $G\left(\mathcal{Q}, T\right)$, and the corresponding Euler-Lagrange equation is:

$$g'\frac{d^4\mathcal{Q}}{dr^4} - g\frac{d^2\mathcal{Q}}{dr^2} + A\theta_s\left(\coth\frac{\theta_s}{T} - \coth\frac{\theta_s}{T_c}\right)\mathcal{Q} + B\mathcal{Q}^3 = 0, \tag{5}$$

with the following boundary conditions:

$$\mathcal{Q} = \begin{cases} \mathcal{Q}_0: & r = \infty \\ -\mathcal{Q}_0: & r = -\infty, \end{cases}$$

$$\mathcal{Q}_0^2 = \frac{-A\theta_s}{B}\left(\coth\frac{\theta_s}{T} - \coth\frac{\theta_s}{T_c}\right).$$

The solution to equation (5) for $g' = 0$ is well-known:

$$\mathcal{Q}(r) = \mathcal{Q}_0\tanh\left[\frac{r}{\mathcal{W}}\right], \tag{6}$$

with $\mathcal{W}$ being the characteristic thickness of the domain wall:

$$\mathcal{W}^2 = 2g/\left[-A\theta_s\left(\coth\frac{\theta_s}{T} - \coth\frac{\theta_s}{T_c}\right)\right] = \frac{2g}{|a|}.$$

The solution for $g' \neq 0$ does not have an analytical form, and can be approximately derived by perturbation methods. The coefficients can be renormalized [1,9], leading to the dimensionless Euler-Lagrange equation:

$$-\mathcal{Q} + \mathcal{Q}^3 = \frac{d^2\mathcal{Q}}{dr^2} - \gamma\frac{d^4\mathcal{Q}}{dr^4}, \tag{7}$$

with $\mathcal{Q}$ redefined in units of $\mathcal{Q}_0$, and $\gamma = g'|a|/g^2$. The solution to this equation, for $\gamma = 0$, is equation (6), with $\mathcal{Q}_0 = 1$ and $\mathcal{W}^2 = 2$. As a first approximation for $\gamma \neq 0$, we can use the same functional form of $\mathcal{Q}$ and treat $\mathcal{W}$ as a variational parameter. In the limit of small r, equation (7) then yields:

$$\mathcal{W}^2 = 1 + \sqrt{1 + 16\gamma} \approx 2 + 8\gamma,$$

which points in the direction of an effective increase in the wall thickness compared to the minimum value of $\mathcal{W}^2 = 2$.

To get a better estimate for the effect of the fourth order gradient term, the trial function can be expanded for $r \ll \mathcal{W}$:

$$\mathcal{Q} = \tanh\left[\frac{r}{\mathcal{W}}\right] + \delta(r), \tag{8}$$

where $\delta(r)$ is a correction function close to the center of the domain wall. We still treat the wall width $\mathcal{W}$ as a variational parameter that is expected to increase with γ. The contribution of $\delta(r)$ in terms of equation (7) is:

$$\begin{aligned} \delta - 3\delta\tanh^2\frac{r}{\mathcal{W}} + \frac{d^2\delta}{dr^2} - \gamma\frac{d^4\delta}{dr^4} = \\ - \left(1 - \frac{2}{\mathcal{W}^2} - \frac{16\gamma}{\mathcal{W}^4}\right)\tanh\frac{r}{\mathcal{W}} \\ - \left(1 - \frac{2}{\mathcal{W}^2} - \frac{40\gamma}{\mathcal{W}^4}\right)\tanh^3\frac{r}{\mathcal{W}} - \frac{24\gamma}{\mathcal{W}^4}\tanh^5\frac{r}{\mathcal{W}}. \end{aligned} \tag{9}$$

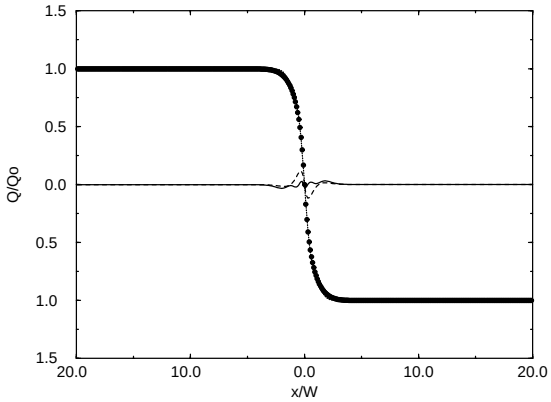

Fig. 1. The numerically obtained data for the twin domain wall profile in the bulk is represented with dots. The best fit using the fourth order Landau-Ginzburg model (8) is represented by a dotted line. Solid line is the difference curve for the fourth order model, and the dashed line is the difference curve for the standard, second order model (6).

The functional form of $\delta(r)$ is clear from the above expression if we write:

$$\delta(r) = (Ar^3 + Br)f(r), \tag{10}$$

with $f(r)$ being a concave function, flat for $r \ll \mathcal{W}$ and approaching 0 rapidly for $r \gg \mathcal{W}$. By Taylor expansion of the hyperbolic tangent, we can calculate for $r \ll \mathcal{W}$:

$$A = -\frac{8\gamma}{\mathcal{W}^7},\ B = \frac{1}{3\mathcal{W}}\left(-1 + \frac{2}{\mathcal{W}^2} + \frac{40\gamma}{\mathcal{W}^4} + \frac{8\gamma}{\mathcal{W}^6}\right)$$

with the condition for $\mathcal{W}(\gamma)$: $\gamma = \dfrac{(\mathcal{W}^2)^3 - 2(\mathcal{W}^2)^2}{\gamma\mathcal{W}^2 + 72}$.

We have fitted the numerical data using both models, described by equations (6, 8), with the $\delta(r)$ taking the form of equation (10), by looking at the value of the strain in the middle of the simulated sample, in order to avoid any surface relaxation effects.

Using the equation (6) we found the best fit for the wall width to be $\mathcal{W} = 10$, measured in unit cells. The fit is apparently very good, but the difference curve shows quite a noticeable discrepancy between the data and the model in the region close to the center of the domain wall (Fig. 1). This discrepancy is a consequence of the fact that the fourth order spatial derivative in equation (5) was neglected ($g' = 0$) in the derivation of the wall profile (Eq. (6)), as discussed above.

When the numerical data was fitted with equation (8) we got much better results, as can be seen from the shape of the difference curve. In this case, we found the wall width to be $\mathcal{W} = 7$, setting $\gamma = 0.3$ and using a Gaussian of appropriate width $\sigma = 6$ as $f(r)$. Hence, the wall profile was found to be:

$$\mathcal{Q} = \tanh\left[\frac{r}{\mathcal{W}}\right] + (Ar^3 + Br)\frac{\mathcal{H}}{\sqrt{2\pi\sigma}}e^{-\frac{1}{2}\left(\frac{r}{\sigma}\right)^2},$$

with all the symbols as defined above, and $\mathcal{H}$ the scaling factor for the height of the Gaussian.

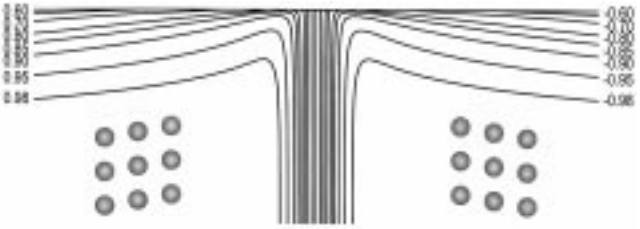

Fig. 2. Distribution of the order parameter $\mathcal{Q}$ at the surface of the lattice (first 50 layers). Lines represent constant $\mathcal{Q}/\mathcal{Q}_0$. There are three lines in the middle of the twin domain wall that are not labeled, they represent the $\mathcal{Q}/\mathcal{Q}_0$ values of 0.40, 0.00, and -0.40 respectively. Notice the steepness of the gradient of $\mathcal{Q}/\mathcal{Q}_0$ through the twin domain wall. The two structures represent sheared twin atomic configurations in the bulk (far from the twin domain wall and surfaces).

The difference in the wall widths for the two different models are expected. The model that includes the fourth order derivative equation (8), yields a lower value for the width of the domain wall, and the effects of the additional factors from equation (10) account for the broadening evident from the fit of the simple model (6).

To conclude, the wall widths we obtained from the simulation are in general agreement with the values for real materials [20–23].

4 Single domain wall and its surface features

The main interest here was the precise determination of the surface features of the twin domain wall. The above presented analytical method based on the Landau-Ginzburg phenomenological model has not been employed to deal with the mesoscopic structure of the twin domain wall at the surface. The mesoscopic features at the surface arise from a solution to a double relaxational problem, consisting of both the relaxation originating in the effects of the free surface and those due to the effects of a domain wall. Each of these problems, on its own, has been successfully treated in the framework of the Landau-Ginzburg model. The two relaxational problems have not been solved concurrently. The complexity of the concurrent treatment arises from the inherent multidimensionality of the problem that includes both surface and domain wall relaxations [24].

Close to the surface the wall apparently widens in a characteristic trumpet-like shape, a consequence of both surface and domain wall origins of the relaxation effects (Fig. 2). We calculated the domain wall width at the surface, using the following expression:

$$\mathcal{Y}_s(x) = \mathcal{Y}_0 + \int_0^x \mathcal{Q}_s(t)dt,$$

where $\mathcal{Y}_s$ is the real space position of the surface particles, $\mathcal{Y}_0$ is the position of the particle at the center of the domain wall, and $\mathcal{Q}_s$ is the order parameter distribution at the surface. This calculation has indicated that there is no appreciable difference between $\mathcal{W}$ and $\mathcal{W}_s$.

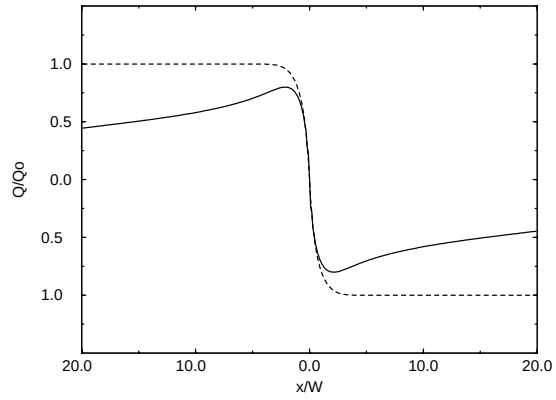

Fig. 3. $\mathcal{Q}_s/\mathcal{Q}_0$ (solid line, proportional to the strain at the surface) and $\mathcal{Q}/\mathcal{Q}_0$ (dashed line, proportional to the strain in the bulk). The widths of the twin domain wall in the bulk, $\mathcal{W}$, and at the surface, $\mathcal{W}_s$, are the same.

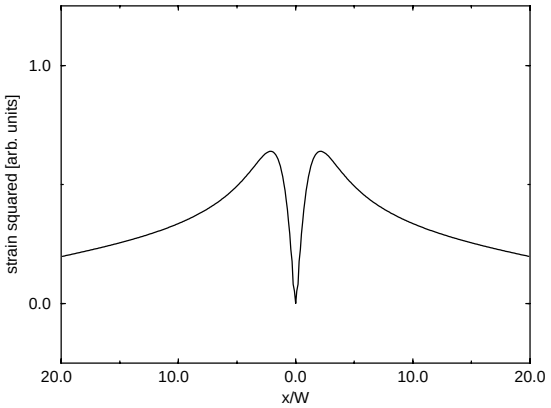

Fig. 4. The square of the order parameter at the surface $\mathcal{Q}_s^2$ related to the chemical potential, and indicative of the areas of maximum decoration, where the distortion of the lattice is at a maximum.

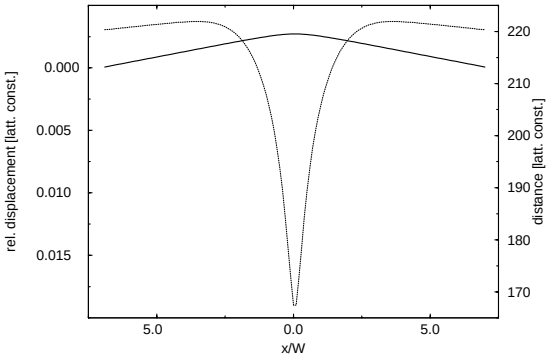

Fig. 5. Surface topography as a solid line with the scale on the right and the groove due to the wall relaxation as a dashed line with the scale on the left. The order of magnitude of surface deformation is three times larger compared to that of the deformation due solely to the domain wall relaxation.

The surface relaxation depth λ was obtained by using the standard expression arising from the thermodynamic Landau-Ginzburg description [25]:

$$\mathcal{Q} = \mathcal{Q}_0\,(1 - e^{-y/\lambda}).$$

Close to the twin domain wall interface with the surface, this expression is modified as a result of the influence of the twin domain wall. The exact description of the modification is a topic of our current research. The magnitude of λ was found to be at a minimum close to the twin domain wall and increasing with distance away from it. This can be seen from Figure 2, where the measure of the surface relaxation is any contour of constant $\mathcal{Q}$. At an infinite distance λ would reach its maximum value $\lambda_{max} = \mathcal{W} = 7$, calculated from the simulation results, measured in lattice constants, which is the surface relaxation depth of the lattice if no twin domain walls are present. Consequently, in materials with microstructure formed by an array of periodic twin domain walls [26], the depth of surface relaxation λ_{array} is suppressed proportionally to the domain wall density, $\lambda_{array} < \lambda_{max}$. The magnitude of the order parameter at the surface $\mathcal{Q}_s$ exhibits exactly the opposite behavior.

The relation between $\mathcal{W}$ and $\mathcal{W}_s$, the domain wall widths in the bulk and at the surface, can most easily be seen if plotted on the same graph. The effect of the surface relaxation is clearly visible as the order parameter at the surface $\mathcal{Q}_s$ never reaches the bulk value $\mathcal{Q}_0$ (Fig. 3).

The distribution of the square of the order parameter $\mathcal{Q}_s^2$ at the surface shows the structure that some of the related experimental works have been reporting [27,28], namely a groove centered at the twin domain wall with two ridges, one on each side.

In addition, the square of the surface order parameter is proportional to the chemical reactivity profile of the twin domain wall interface at the surface [29,30]. Intuitively, one would expect the chemical reactivity of the surface to be the largest at the center of the twin domain wall, falling off as the distance from the center of the wall increases. Contrary to the expected behavior, chemically most reactive areas are at the sides of the twin domain wall, and the center of the twin domain wall at the surface is the least reactive area. The reactivity, proportional to $\mathcal{Q}_s^2$, does indeed fall off as the distance from the center of the wall increases, as expected, but only after it has reached a maximum at a distance of $\sim 3\mathcal{W}$ (Fig. 4) from the center of the domain wall. If such a structure is exposed to particle adsorption (*e.g.* in the MBE growth of thin films on twinned substrates) we expect the sticking coefficient to vary spatially. In one scenario, adsorption may be enhanced on either side of the wall while being reduced at the center.

The real space topography of the surface is determined by both sources of relaxation – twin domain wall and the surface. These are distinct and when considered separately, we found the effect due to the wall relaxation larger by about three orders of magnitude then that due to the surface relaxation (Fig. 5).

The lattice features in the bulk are dominated exclusively by the domain wall relaxation, as the surfaces are too far away. This has provided us with a precise description of the relaxation due exclusively to the twin domain wall. By effectively removing this from the relaxed surface,

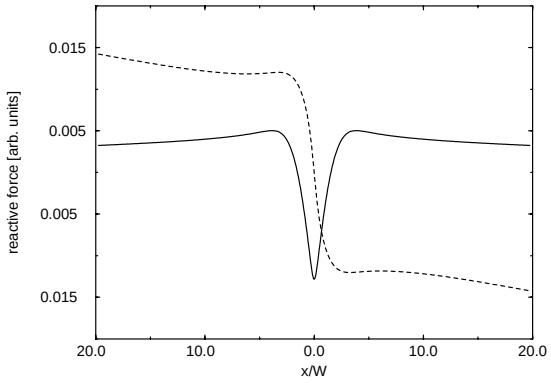

Fig. 6. Distribution of the normal (solid line) and lateral (dashed line) response to normal displacement of the surface particles. Lateral response can be useful for observing the domain structure, while normal response can be useful for the observation of twin domain walls.

we were left with the effects of the surface relaxation only. These yield a groove, centered at the twin domain wall, without any extra features (Fig. 5). One recent analytical work [24], has in fact considered only the surface relaxation effects, while the much bigger wall relaxations were frozen, and a groove at the surface was predicted, just as the one we obtained by removing the wall relaxation effects. It is important to note that the groove only appears when the domain wall relaxation is ignored, yielding inaccurate description of the surface topology, as the effects due to the wall relaxation are three orders of magnitude larger (displacements of particles due to the surface relaxation are $\sim 10^{-3}a$, whereas displacements due to the wall relaxation are $\sim a$). In fact, the wall relaxation completely dominates the topography of the twin domain wall surface structure, entirely masking the groove-like effects originating in the surface relaxation, thus creating the surface rounding centered at the twin domain wall (Fig. 5). A recent AFM-tapping mode study [14] has identified this feature. It reports a "nose" effect on the surface, that we have not been able to verify.

In the attempt to predict the possible experimental results of AFM investigations of the surface structure of the twin domain wall, we emulated the effect that the tip at the end of an AFM cantilever has on the surface of the material. This we did by displacing each particle in the surface layer by $10^{-8}a$ in the $-\mathbf{y}$ direction. We then calculated the lateral and normal components of the reactive force. The lateral force distribution shows a dependence similar to that of the order parameter $\mathcal{Q}_s$ (Fig. 6). The normal force distribution has a profile similar to that of the square of the order parameter, $\mathcal{Q}_s^2$, with ridges on both sides of a groove (Fig. 6).

The change in the sign of the order parameter at the surface has been observed (for ferroelectrics) by using a mode of imaging developed for the detection of static surface charge [16]. For ferroelastics discussed here, this corresponds to the profile of the lateral reactive force. The SFM non-contact dynamic mode images [17] would correspond to the distribution of the normal reactive force. The divergence of the lateral force distribution away from the center of the wall can be attributed to the simulated infinite extension of the lattice. In the simulated array, the lateral component of the force reached a finite value between two adjacent domain walls.

These results can be used as a guidance for the future experimental work. In order to determine the twin domain wall width $\mathcal{W}$ in the bulk, one only needs to determine the characteristic width $\mathcal{W}_s$ of the surface structure of the domain wall. Previously, these features of the twinning materials were investigated using mainly X-ray techniques. In fact, the only necessary information for the determination of the twin domain wall width $\mathcal{W}$ are the real space positions of the particles in the surface layer.

References

1. E.K.H. Salje, *Phase transitions in ferroelastic and coelastic crystals* (Cambridge University Press, 1993).
2. G. van Tendeloo *et al.*, Solid State Commun. **63**, 389 (1987).
3. A. Rosova *et al.*, Physica C **214**, 247 (1993).
4. A. Nouruzi-Khoransani *et al.*, J. Cryst. Growth **98**, 461 (1989).
5. S. Marais *et al.*, Phys. Rev. Lett. **66**, 2480 (1991).
6. K. Parlinski *et al.*, J. Phys.: Condens. Matter **5**, 497 (1993).
7. E.K.H. Salje *et al.*, J. Phys.: Condens. Matter **5**, 4775 (1993).
8. A.M. Bratkovsky *et al.*, J. Phys.: Condens. Matter **6**, 3679 (1994).
9. I. Tsatskis *et al.*, J. Phys.: Condens. Matter **6**, 11027 (1994)
10. S. Amelinckx, D. van Dyck, J. van Landuyt, G. van Tendeloo, *Handbook of Microscopy* (VCH Verlagsgesellschaft mbH, 1997).
11. E.K.H. Salje, Phase Trans. **55**, 37 (1995).
12. J. Chrosch, E.K.H. Salje, Physica C **225**, 111 (1994).
13. D. Viehland *et al.*, Phil. Mag. **71**, 205 (1995).
14. D. Bosbach *et al.*, J. Phys.: Condens. Matter **9**, 8397 (1997).
15. C. Schönenberger, Phys. World **10**, 25 (1997).
16. F. Saurenbach, B.D. Terris, Appl. Phys. Lett. **56**, 1703 (1990).
17. R. Lüthi *et. al.*, J. Appl. Phys. **74**, 7461 (1993).
18. Z.W. Hu *et al.*, J. Phys. D: Appl. Phys. **28**, 189 (1995).
19. B. Houchmanzadeh *et al.*, J. Phys.: Condens. Matter **4**, 9779 (1992).
20. K.R. Locherer *et al.*, Phil. Trans. R. Soc. Lond. A **354**, 2815 (1996).
21. B. Wruck *et al.*, Phase Trans. **48**, 135 (1994).
22. E.K.H. Salje, Phase Trans. **55**, 37 (1995).
23. S.A. Hayward *et al.*, Eur. J. Mineral. **8**, (1996).
24. I. Rychetský, J. Phys.: Condens. Matter **9**, 4583 (1997).
25. B. Houchmanzadeh *et al.*, Phase Trans. **38**, 77 (1992).
26. E.K.H. Salje, K. Parlinski, Supercond. Sci. Technol. **4**, 93 (1991).
27. S. Tsunekawa *et al.*, Materials Trans. JIM, **36**, 1188 (1995).
28. Tung Hsu, J.M. Cowley, Ultramicroscopy **55**, 302 (1994).
29. R.V. Mehta *et al.*, J. Imaging Sci. Tech. **40**, 77 (1996).
30. B. Houchmanzadeh *et al.*, J. Phys.: Condens. Matter **3**, 5163 (1991).